NANO LETTERS

pubs.acs.org/NanoLett
Letter

Observation of Boron Vacancy Concentration in Hexagonal Boron Nitride at Nanometer Scale

Jun Kikkawa,* Chikara Shinei, Jun Chen, Yuta Masuyama, Yuichi Yamazaki, Teruyasu Mizoguchi, Koji Kimoto, Takashi Taniguchi, and Tokuyuki Teraji

Cite This: https://doi.org/10.1021/acs.nanolett.5c02988

ABSTRACT: Negatively charged boron vacancy (V_B^-) ensembles in hexagonal boron nitride (h-BN) have attracted considerable attention as a promising platform for quantum sensing. Current challenges include the experimental validation of the spatial distribution and electronic states of optically active V_B^- and optically inactive neutral boron vacancy (V_B^0) defects. To address these issues, we employ electron energy loss spectroscopy (EELS) combined with scanning transmission electron microscopy (STEM) using monochromated 30-keV electrons, effectively reducing background interference. This approach unveils distinct spectral peaks at 2.5 and 1.9 eV, corresponding to V_B^- and V_B^0 defects, respectively. Furthermore, we achieve nanometer-scale concentration mapping for V_B^- and V_B^0 defects, advancing insights into spin defect configurations crucial for optimizing quantum sensor performance.

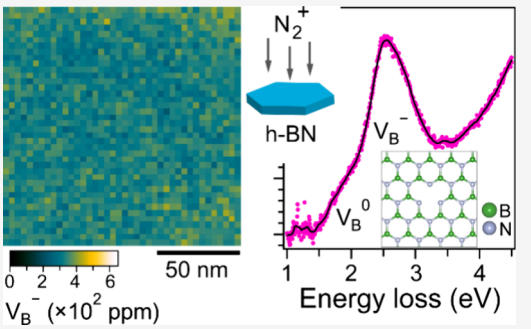

KEYWORDS: *hexagonal boron nitride, boron vacancy, electron energy loss spectroscopy, scanning transmission electron microscopy, frist-principles simulation*

Quantum sensors hold considerable potential for measuring a wide range of physical and chemical properties, providing exceptional resolution and precision.[1,2] Ensembles of color centers (i.e., point defects caused by vacancies and impurities) in hexagonal boron nitride (h-BN) are promising platforms for next-generation quantum sensors as post negatively charged nitrogen-vacancy (NV^-) ensembles in diamond.[3,4] h-BN is a two-dimensional material with a wide bandgap at ∼ 6 eV,[5,6] and has the advantages of easy integration into quantum devices, high photon extraction efficiency, and photon wavelength diversity.[7,8] Negatively charged boron vacancies (V_B^-), antisite nitrogen vacancies (N_BV_N), and carbon-based defects are color centers generating luminescence at ∼1.5,[9−13] ∼2.0,[14,15] and ∼4.1 eV,[16−20] respectively. In particular, the V_B^- centers exhibit spin-dependent photon emission at room temperature, a desirable property for quantum sensing.[9−13] The spatial V_B^- distribution uniformity, V_B^- concentration, and the distance between individual V_B^- defects are fundamental properties, in addition to the crystallinity and purity of h-BN, for determining spatial resolution and sensitivity in quantum sensors. Ion or electron irradiation on h-BN generates V_B^- defects,[9−13] and can simultaneously generate neutral born vacancies (V_B^0) and other types of defects,[21−27] which coexist with intrinsic impurity-related defects.[14−20,28] Direct observations have shown that electron and He^+ ion irradiation preferentially generate V_B defects rather than V_N defects.[25−27] However, the distribution, concentration, and spacing of V_B^- and V_B^0 defects are as yet not fully understood because of the absence of a standardized measurement method at the nanometer scale, especially for optically inactive V_B^0. Furthermore, despite the first-principles simulations of the electronic structures of V_B^- and V_B^0 defects,[17,29−31] experimental validation remains necessary. Therefore, it is crucial to measure the arrangement and electronic states of V_B^- and V_B^0 defects.

Electron energy loss spectroscopy (EELS) combined with scanning transmission electron microscopy (STEM) enables probing the subgap states of lattice defects and the chemical bonding states at defect sites.[32−35] However, measuring the detailed EELS spectral structure from point defects in bulk crystals presents a significant challenge, because of the low concentration of point defects ($\lesssim 10^3$ ppm) and the weakness of EELS signals compared with other intrinsic signals. Three types of background intensity can hinder the detection of EELS signals of defect states. The first is the tail of the zero-loss peak (ZLP, i.e., elastic scattering peak), whose signal can become dominant even in several eV region in EELS. A smaller energy spread of the incident electrons evaluated with full width at half-maximum (fwhm) or more appropriately at 10^{-n}

Received: June 6, 2025
Revised: August 19, 2025
Accepted: August 19, 2025

https://doi.org/10.1021/acs.nanolett.5c02988
Nano Lett. XXXX, XXX, XXX−XXX

($n \geq 1$) of the ZLP,[36] is required to reduce the contribution of the ZLP tail. The second is EELS signals, which can appear at around several eVs owing to the generation of Cherenkov radiation.[37] This radiation can be reduced or ignored by lowering the energy of incident electrons or by using a thinner specimen.[32,33,38] The third is detector noise. It is very important to reduce readout noise in addition to gain noise so that weak signals are not buried in their noise.

In this study, to measure electronic states of V_B^- and V_B^0 defects in h-BN by EELS, we use monochromated 30-keV electrons, reducing the fwhm of the ZLP to 40 meV,[39] and suppressing Cherenkov radiation.[32,33,38,40] To detect scattered electrons in EELS, we use a charge-coupled-device (CCD) camera with a high-sensitivity scintillator optimized for 30-keV electrons,[39] and the readout noise reduction scheme.[41,42] EELS in combination with first-principles simulations revealed a high peak at 2.5 eV with enhanced intensity appearing at the shoulder position of 1.9 eV, which are respectively assigned to signals from V_B^- and V_B^0 defects. Furthermore, we obtain the concentration maps for V_B^- and V_B^0 defects at the nanometer scale.

h-BN single crystals were grown using a temperature gradient method at a high pressure,[43] and their flakes with thicknesses of 30−200 nm were prepared using a tape-peeling method (details of the specimen preparation and experimental methods are described in Supporting Information). The h-BN flakes were dispersed on a holey carbon-film-supported copper grid and then irradiated with a 40-keV nitrogen ion (N_2^+) beam along the *c*-axis at a total dose of 1×10^{15} cm^{-2} at room temperature,[11] as shown in Figure 1a. Figure 1b shows the photoluminescence (PL) spectra of the pristine and irradiated h-BN flakes at room temperature with an incident photon energy of 2.33 eV. PL occurs with a peak maximum at 1.53 eV (=810 nm) only after the irradiation, indicating the formation of optically active V_B^- defects, as observed in previous studies.[9−13] Figure 1c shows the optically detected magnetic resonance (ODMR) spectrum of the irradiated h-BN flake. ODMR occurs at a microwave frequency of ∼3.5 GHz after the irradiation, corresponding to a ground state zero-field splitting between spin states $m_s = 0$ and $m_s = \pm 1$ for V_B^- in h-BN.[4,9] Figure 1d displays the EELS spectra of the pristine and irradiated h-BN flakes below 6.2 eV. Two characteristic EELS intensities appear in the subgap region only for the irradiated h-BN flake as indicated by the arrows (Figure 1d). One is an asymmetric signal centered at ∼2.5 eV and the other is a continuous intensity distribution ranging from 3.8 to 5.9 eV. These EELS intensities reflect the density of states (DOS) of the defect levels introduced by the irradiation. The asymmetric 2.5 eV signal was more clearly observed in flakes thicker than ∼100 nm. In the range of 6−30 eV, there is no marked difference in EELS profiles between the pristine and irradiated h-BN flakes (Figure S1a). In addition, no marked changes were observed at the N *K* edge after the irradiation; only a slightly asymmetric broadening of the peak at 191.8 eV was detected at the B *K* edge (Figures S1b and S1c), suggesting the formation of nitrogen vacancies (see details in Supporting Information).[44] We also observed cathodoluminescence (CL) at approximately 4.1 eV (Figure S2), which occurred depending on the measurement position for both pristine and irradiated flakes. This indicates the presence of carbon-related defects in the original h-BN crystal.[16−20] As the energy levels associated with these defects lie outside the energy range of interest (i.e., 1.5−3.5 eV), it is appropriate to focus exclusively on the V_B^- and V_B^0 defects hereafter (see details in Supporting Information).

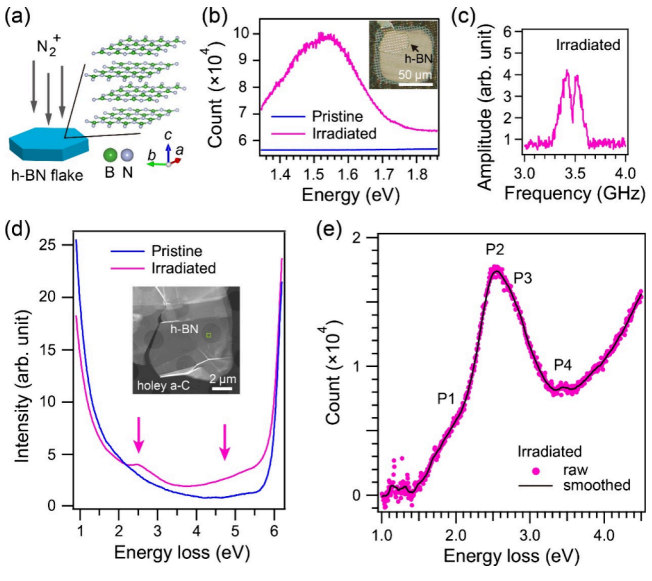

Figure 1. (a) Illustration of N_2^+ ion irradiation of h-BN flake. (b) PL spectra of pristine and irradiated h-BN flakes. (c) ODMR spectrum of irradiated h-BN flake. (d) EELS spectra of pristine and irradiated h-BN flakes. The inset optical microscopy and annular dark-field STEM images in (b) and (d) respectively show the h-BN flakes on a holey a-C film. (e) EELS spectrum after subtraction of the ZLP tail for the irradiated h-BN flake in (b), revealing four characteristic intensity peaks labeled P1−P4. Row data (solid circle) and smoothed profile (solid line).

To identify fine structures of the 2.5 eV asymmetric signal in Figure 1d, we conducted EELS with a high energy resolution (i.e., fwhm of the ZLP, 40 meV). By scanning the electron probe in steps of 3.6 nm in 143 nm-square areas in the irradiated h-BN flake, we obtained 1600 single EELS spectra. By summing the single spectra and subtracting the background intensity mainly due to the ZLP tail with a power-low fit (Figure S3), we found that the asymmetric 2.5 eV signal is composed of four characteristic intensities, as shown in Figure 1e. The high intensity peak P2 locates at 2.5 eV, overlapping with relatively low intensity peaks labeled P1 at 1.9 eV, P3 at 2.9 eV, and P4 at 3.45 eV. The appearance of the intense signal at 2.5 eV in EELS is consistent with the maximum absorption at ∼2.6 eV in PL excitation measurements for V_B^- defects in h-BN.[10] Note that the asymmetric 2.5 eV signal is weaker than intrinsic bulk signals. For instance, the EELS intensity of the 2.5 eV signal (i.e., integrated intensity in the range of 1.34−3.34 eV) is approximately 10^{-1} of that of optical phonons (i.e., integrated intensity in the range of 0.13−0.28 eV), despite the 13-fold difference in integration range (Figure S4).

To understand the fine structures of the 2.5 eV asymmetric signal in Figure 1e, we conducted first-principles simulations (details of the calculation methods are described in Supporting Information). Figures 2a−2c show the electronic DOS values of h-BN crystals without defects, with a V_B^- defect, and with a V_B^0 defect, respectively (see Figure S5 for a wider energy range). Occupied and unoccupied states are filled and blank, while up- and down-spin states are displayed in the upper and lower side, respectively. The three DOS diagrams are aligned with the 2s levels (Figure S5). The positions of VBM and CBM in Figures 2b and 2c denote those for the perfect crystal

https://doi.org/10.1021/acs.nanolett.5c02988
Nano Lett. XXXX, XXX, XXX−XXX

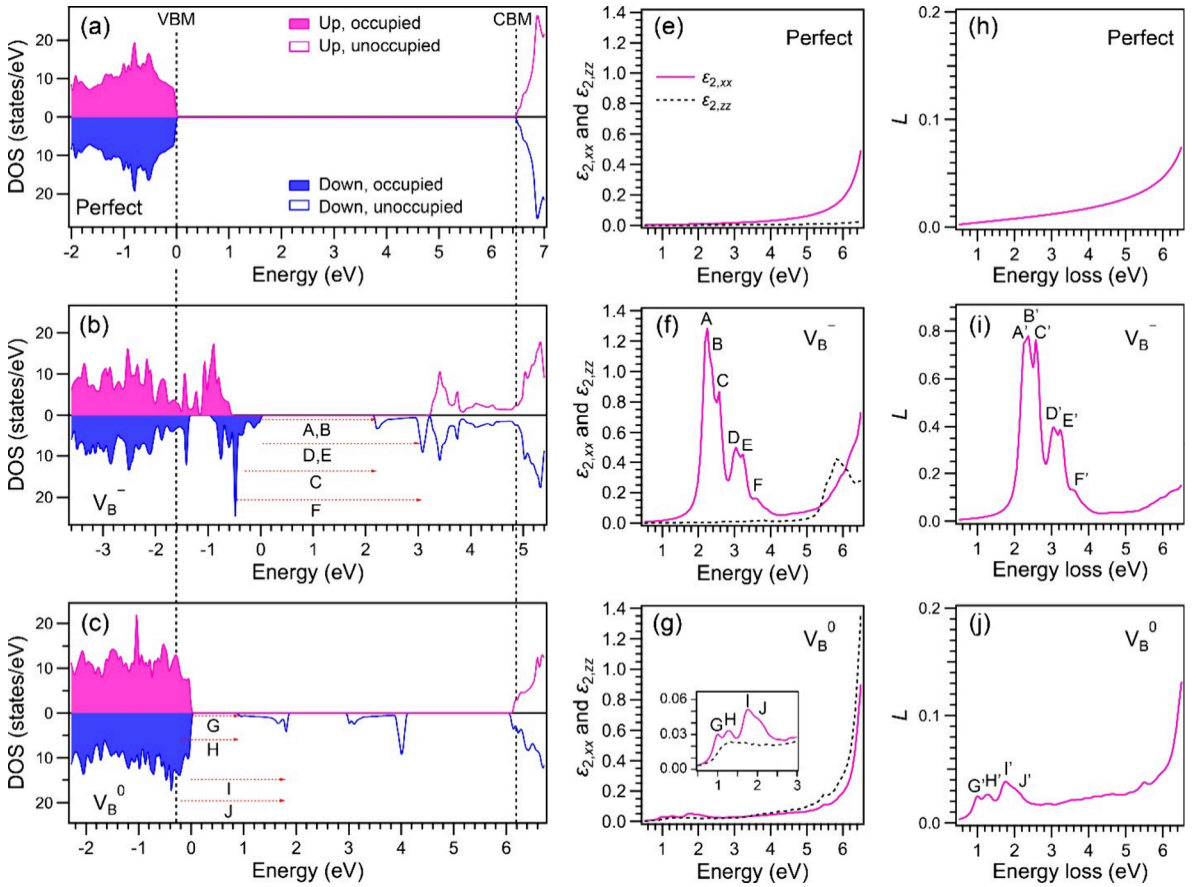

Figure 2. First-principles simulations. [(a)−(c)] DOS values of h-BN crystals without defects, with a V_B^- defect, and with a V_B^0 defect, respectively. The filled and blank areas are the occupied and unoccupied states, respectively. The upper and lower sides are the up- and down-spin states, respectively. [(e)−(g)] Imaginary parts of dielectric function, $\varepsilon_{2,xx}$ (solid line) and $\varepsilon_{2,zz}$ (dashed line) for perfect crystal in (e), V_B^- in (f), and V_B^0 in (g). Intensities in $\varepsilon_{2,xx}$ denoted by A−F in (f) and G−J in (g) originate from electron excitations indicated by A−F in (b) and G−J in (c), respectively. [(h)−(j)] Loss functions (L) for perfect crystal in (h), V_B^- in (i), and V_B^0 in (j). Intensities in L denoted by A′−F′ in (i) and G′−J′ in (j) predominantly reflect the intensities in $\varepsilon_{2,xx}$ denoted by A−F in (f) and G−J in (g).

(Figure 2a). As shown in Figures 2b and 2c, subgap states between VBM and CBM differ largely depending on whether the charge of V_B is − 1 or zero. The diagonal components of the dielectric tensor perpendicular and parallel to the c-axis are written as $\boldsymbol{\varepsilon}_{xx} = \varepsilon_{1,xx} + i\varepsilon_{2,xx}(=\boldsymbol{\varepsilon}_{yy})$ and $\boldsymbol{\varepsilon}_{zz} = \varepsilon_{1,zz} + i\varepsilon_{2,zz}$, respectively. Figures 2e−2g show the imaginary parts $\varepsilon_{2,xx}$ and $\varepsilon_{2,zz}$ for the perfect crystal, the V_B^- defect, and the V_B^0 defect, respectively (see Figure S6 for a wider energy range and real parts). The imaginary parts represent absorption. Note that $\varepsilon_{2,xx}$ for the V_B^- defect is intense with fine structures denoted as A−F in the 2.0−4.0 eV range (Figure 2f). This indicates that electronic excitations at 2.0−4.0 eV in the *ab*-plane direction are dominant compared with those along the c-axis. For the V_B^0 defect, $\varepsilon_{2,xx}$ has a relatively low intensity and fine structures denoted as G−J in the 0.5−2.5 eV range (Figure 2g), whereas there is no characteristic intensity in $\varepsilon_{2,xx}$ and $\varepsilon_{2,zz}$ for the perfect crystal because of the absence of subgap states (Figure 2e). The A−F peaks in Figure 2f and the G−J peaks in Figure 2g originate from the electron excitations between subgap states, A−F in Figure 2b and G−J in Figure 2c. The loss function L when the electron incident direction is parallel to the c-axis and the convergence angle $\alpha = 0$ is calculated as[45]

$$L = -\mathrm{Im}\left[\frac{1}{2\boldsymbol{\varepsilon}_{zz}}\ln\left(1 + \frac{\boldsymbol{\varepsilon}_{zz}\beta^2}{\boldsymbol{\varepsilon}_{xx}\theta_E^{\,2}}\right)\right]$$

$\theta_E = \Delta E/2E_0$ in nonrelativistic form, where E_0 (=30 keV) and ΔE respectively represent the incident energy and energy loss of the primary electron: $\theta_E = 4.2 \times 10^{-2}$ mrad for $\Delta E = 2.5$ eV. Considering that the electron probe used in STEM−EELS has α ($\neq 0$), β is approximately replaced with $\beta^* = \sqrt{\alpha^2 + \beta^2}$ to calculate L (details are described in Supporting Information). Figures 2h−2j show L for the perfect crystal, the V_B^- defect, and the V_B^0 defect, respectively. The profile of L mainly reflects that of $\varepsilon_{2,xx}$. The A′−F′ peaks in Figure 2i and the G′−J′ peaks in Figure 2j reflect the A−F peaks in Figure 2f and the G−J peaks in Figure 2g, respectively. This is because $\varepsilon_{2,xx}$ in L becomes dominant when $\theta_E \ll \beta$ and also because $\varepsilon_{2,zz}$ is originally small. Reflecting the intensities of $\varepsilon_{2,xx}$ in L for the V_B^- and V_B^0 defects (Figures 2f and 2g), the intensity of L for the V_B^- defect [L (V_B^-)] in the range including the A′−F′ peaks (Figure 2i) is higher than that L for the V_B^0 defect [L (V_B^0)] in the range including the G′−J′ peaks (Figure 2j). Figures 2i and 2j also suggest that the EELS intensity in the 4−6 eV range in Figure 1d originates from other types of defects and partly from the V_B^- defects. Figure 3 shows plots of L (V_B^-) and L (V_B^0) with coefficients of 0.16 and 0.84, respectively, and their linear combination, 0.16 L (V_B^-) + 0.84 L (V_B^0), where L was plotted so that the linear combination profile matched the smoothed EELS spectrum (Figure 1e) (see Figure S8 for the method of determining the coefficients). The good agreement between

https://doi.org/10.1021/acs.nanolett.5c02988
Nano Lett. XXXX, XXX, XXX−XXX

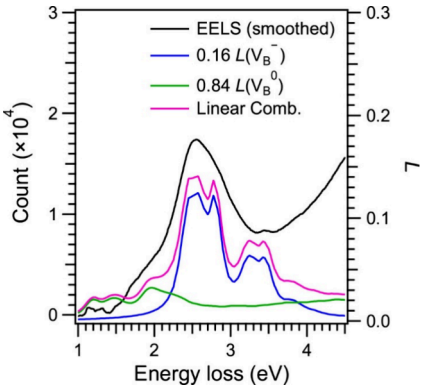

Figure 3. Plots of the loss function L for V_B^- (blue) and V_B^0 (green) in Figure 2 with factors of 0.16 and 0.84, respectively, their linear combination (magenta), and smoothed EELS spectrum (black) in Figure 1e.

the linear combination and the EELS spectrum enables the assignment of the origin of the P1−P4 peaks in EELS and reveals the concentration ratio of the V_B^0 defects to the V_B^-defects, V_B^0/V_B^- is 5.3 as the average value within the measured 143 nm-square area. The intense P2 peak in EELS corresponds to the A′ and B′ peaks in L (V_B^-), and, thus, the electron excitations A and B in Figure 2b. The P3 and P4 peaks correspond to the C′ and E′ peaks in L (V_B^-), whereas the P1 peaks correspond to the I′ peak in L (V_B^0). The finding that the optically inactive V_B^0 coexists with the optically active V_B^- implies that adjusting the charge state from 0 to − 1 can increase the V_B^- concentration through electron injection.[22,46] Figure 4 shows a schematic unifying our understanding from

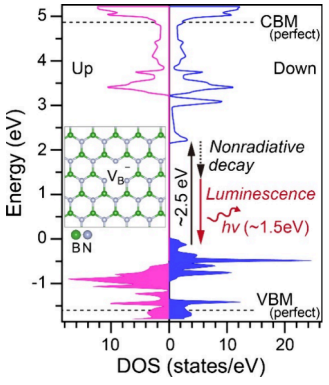

Figure 4. Schematic of the 2.5 eV electron excitation (i.e., absorption) and 1.5 eV luminescence accompanied by nonradiative decay at the V_B^- defect in h-BN, illustrated in the DOS schematic of the ground states.

the results of PL, EELS, and first-principles simulations in this study and PL excitation in a previous study for V_B^-.[10] As illustrated in the DOS schematics of the ground state for V_B^- (Figure 4), the 1.53 eV PL occurs as an electronic relaxation process after the 2.5 eV excitation (i.e., absorption in EELS and PL excitation) between the occupied and unoccupied defect states. The remaining energy of approximately 1 eV is attributed to nonradiative relaxation.

To evaluate the absolute concentrations of V_B^- and V_B^0 by EELS, we utilize the vacancy concentration in the supercell for first-principles simulations, which is 13889 ppm for both V_B^- and V_B^0. Using the integrated intensities for V_B^- and V_B^0 (i.e., V_B^- + V_B^0) in the range of 1.0−3.0 eV and the π-plasmon in the loss functions and those in the EELS spectrum, we estimated the average concentration of V_B^- + V_B^0 as approximately 2000 ppm (details are given in Figure S9). We assumed that the intensity ratio of V_B to the π plasmon in EELS is proportional to the V_B concentration. Then, the average V_B^- and V_B^0 concentrations are approximately estimated as 300 and 1700 ppm, using the coefficients 0.16 and 0.84 (Figure 3), respectively. The average V_B^- concentration can be evaluated directly using the integrated intensities for V_B^- in the range of 2.3−3.0 eV, resulting in 300 ppm as well (details are given in Figure S10). By implementing this method for the original 1600 single spectra from the 143 nm-square area (i.e., 40 × 40 pixels), we obtained the concentration map of V_B^- and its histogram, as shown in Figures 5a and 5b, respectively. The V_B^- concentration is nearly uniform without significant segregation (Figure 5a). The Gaussian fit in Figure 5b provides the center and standard deviation of 330 ± 33 ppm, which is close to the average value of 300 ppm estimated above. Figures 5c and 5d respectively show the map of the concentration ratio of V_B^0 to V_B^- (i.e., V_B^0/V_B^-) and its histogram, where the V_B^0/V_B^- ratio at each pixel was obtained using the integrated intensities in the ranges of 1.7−2.0 eV for V_B^0 and 2.3−2.6 eV for V_B^- (Figure S8a). The V_B^0/V_B^- map represents the distribution of the charge state ratio (i.e., 0 to − 1). The negative values of the V_B^0/V_B^- ratio for several pixels are due to the excess removal of ZLP tail signals and the low signal-to-nose ratio. The Gaussian fit in Figure 5d gives V_B^0/V_B^-=5.0 ± 1.7, which closely matches the average V_B^0/V_B^-=5.3 obtained after integrating the 1600 single spectra described above. By multiplying the V_B^- map (Figure 5a) and the V_B^0/V_B^- map (Figure 5c), we also obtained the concentration map of V_B^0 and its histogram as shown in Figures 5e and 5f, respectively. The Gaussian fit in Figure 5f provides the center and standard deviation of 1647 ± 648 ppm, which is close to the average value of 1700 ppm estimated above. Figures 5g−5i show plots of typical single EELS spectra at 1 pixel (3.6 nm-square areas) in Figure 5c with the V_B^0/V_B^- values of 1.4, 5.0, and 7.1, respectively. The smoothed line profiles certainly reveal the increase in P1 intensity at ∼ 1.9 eV from Figures 5g to 5i. Regarding the spatial resolution of the maps (Figure 5), the diameter and scan step of the electron probe we used were 0.6−0.7 and 3.6 nm, respectively, whereas the effective diameter considering the delocalization of EELS around 2.5 eV was estimated to be 8 nm.[37] Thus, the maps in Figure 5 are blurred by approximately 2 × 2 pixels compared with the actual intensity distribution.

Finally, we briefly discuss the quantitative aspects of the concentration maps in Figure 5. The primary concern lies in the comparison between the electron arrival time interval Δt at the electron probe position in STEM−EELS and the lifetime τ from the excited state back to the ground state for V_B^- and V_B^0. In this study, Δt was 1.3 ns (i.e., the probe current of ∼120 pA) and the exposure time at each pixel was 0.6 s in Figure 5. The excited state for V_B^- returns to the ground state predominantly via a singlet metastable state.[31,47] The lifetime of this metastable state is approximately 10−30 ns at room temperature, making τ longer than this,[47−50] whereas the lifetime of V_B^0 remains unknown. This suggests the potential for underestimating the V_B^- concentration during EELS measurement at each pixel. The measurement was probably performed with a certain fraction of V_B^- in the metastable state, specifically with a reduced concentration of V_B^-. Reducing the probe

https://doi.org/10.1021/acs.nanolett.5c02988
Nano Lett. XXXX, XXX, XXX−XXX

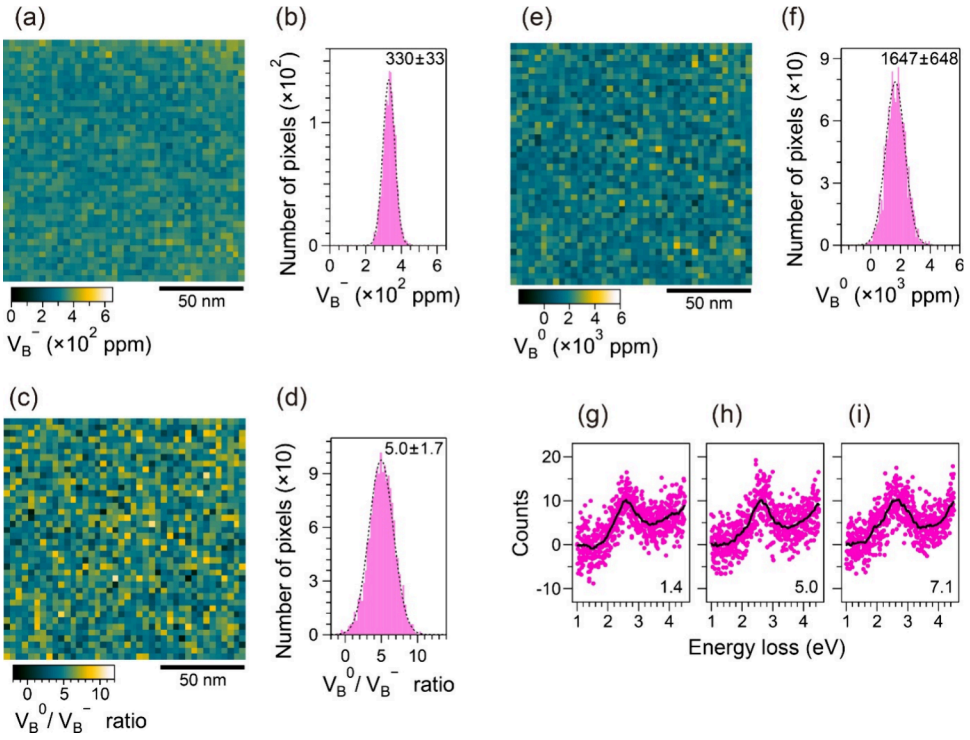

Figure 5. Concentration maps of vacancies in the irradiated h-BN flake. The V_B^- map in (a) and its histogram in (b). The V_B^0/V_B^- ratio map in (c) and its histogram in (d). The V_B^0 map in (e) and its histogram in (f). All maps have the same area. The centers and standard deviations for Gaussian fits in the histogram are 300 ± 33 ppm, 5.0 ± 1.7, and 1647 ± 648 ppm in (b), (d), and (f), respectively. [g–h] Typical single EELS spectra at 1 pixel (3.6 nm-square areas) with the V_B^0/V_B^- ratios of 1.4, 5.0, and 7.1 in (g), (h), and (i), respectively.

current to below 1 pA and increasing the exposure time would resolve this issue, although it is expected to result in a lower signal-to-noise ratio of the spectrum, making measurements more challenging. Alternatively, when the τ of V_B^0 is comparable to that of V_B^-, the V_B^0/V_B^- ratio can be considered quantitative despite the underestimation of the respective absolute densities. In any case, the optimization of EELS conditions and a more precise quantitative evaluation of both relative and absolute densities remain future challenges.

In summary, in this study, we investigated the intricate characteristics of optically active V_B^- and optically inactive V_B^0 defects in nitrogen-ion irradiated h-BN by STEM–EELS with monochromated 30-keV electrons and first-principles simulations. EELS played a pivotal role in identifying the subgap states resulting from the irradiation, distinguishing distinct spectral peaks at 2.5 and 1.9 eV corresponding to V_B^- and V_B^0 defects, respectively. The concentrations of V_B^- and V_B^0 defects were estimated as approximately 300 and 1700 ppm on average, respectively. We also accomplished the concentration mapping of these defects at the nanometer scale, which revealed their near-uniform distribution without significant segregations. As a future challenge, it is necessary to optimize EELS conditions by considering the lifetime τ to avoid the underestimation of defect concentration. Such optimization is imperative for precise quantitative assessments, as it provides indispensable insights that are vital for the future application of h-BN in quantum technology sectors.

■ ASSOCIATED CONTENT

Supporting Information

The Supporting Information is available free of charge at https://pubs.acs.org/doi/10.1021/acs.nanolett.5c02988.

Details of experimental method, first-principles simulations, other possible defects, loss function calculation, and additional figures (PDF)

■ AUTHOR INFORMATION

Corresponding Author

Jun Kikkawa − *National Institute for Materials Science, Tsukuba 305-0044, Japan;* orcid.org/0000-0003-0659-1844; Email: kikkawa.jun@nims.go.jp

Authors

Chikara Shinei − *National Institute for Materials Science, Tsukuba 305-0044, Japan*

Jun Chen − *National Institute for Materials Science, Tsukuba 305-0044, Japan*

Yuta Masuyama − *National Institutes for Quantum Science and Technology, Takasaki 370-1292, Japan*

Yuichi Yamazaki − *National Institutes for Quantum Science and Technology, Takasaki 370-1292, Japan*

Teruyasu Mizoguchi − *Institute of Industrial Science, The University of Tokyo, Tokyo 153-8505, Japan;* orcid.org/0000-0003-3712-7307

Koji Kimoto − *National Institute for Materials Science, Tsukuba 305-0044, Japan;* orcid.org/0000-0002-3927-0492

Takashi Taniguchi − *National Institute for Materials Science, Tsukuba 305-0044, Japan;* orcid.org/0000-0002-1467-3105

Tokuyuki Teraji − *National Institute for Materials Science, Tsukuba 305-0044, Japan*

Complete contact information is available at: https://pubs.acs.org/10.1021/acs.nanolett.5c02988

https://doi.org/10.1021/acs.nanolett.5c02988
Nano Lett. XXXX, XXX, XXX−XXX

Author Contributions

J.K. and T. Teraji conceived and directed the project. T. Taniguchi made the h-BN crystal. Y.M. and Y.Y. conducted the nitrogen-ion irradiation. J.K. conducted EELS experiments and analyses. C.S., Y.Y., and J.C. measured PL, ODMR, and CL spectra, respectively. T.M. conducted first-principles simulations. All authors have discussed the experimental and simulated results. J.K. wrote the manuscript with the support of all the authors.

Notes

The authors declare no competing financial interest.

■ ACKNOWLEDGMENTS

J.K. thanks Y. Moronaga (NIMS) for specimen preparations and J. Inoue (NIMS) for fruitful discussion. This work was partly supported by JSPS KAKENHI Grant Nos. JP22H01959 and JP23H02052 and World Premier International Research Center Initiative (WPI), MEXT, Japan.

■ REFERENCES

(1) Taylor, J. M.; Cappellaro, P.; Childress, L.; Jiang, L.; Budker, D.; Hemmer, P. R.; Yacoby, A.; Walsworth, R.; Lukin, M. D. High-Sensitivity Diamond Magnetometer with Nanoscale Resolution. *Nat. Phys.* **2008**, *4* (10), 810−816.

(2) Aslam, N.; Pfender, M.; Neumann, P.; Reuter, R.; Zappe, A.; Fávaro de Oliveira, F.; Denisenko, A.; Sumiya, H.; Onoda, S.; Isoya, J.; et al. Nanoscale Nuclear Magnetic Resonance with Chemical Resolution. *Science* **2017**, *357* (6346), 67−71.

(3) Tetienne, J. P. Quantum Sensors Go Flat. *Nat. Phys.* **2021**, *17* (10), 1074−1075.

(4) Gottscholl, A.; Diez, M.; Soltamov, V.; Kasper, C.; Krauße, D.; Sperlich, A.; Kianinia, M.; Bradac, C.; Aharonovich, I.; Dyakonov, V. Spin Defects in hBN as Promising Temperature, Pressure and Magnetic Field Quantum Sensors. *Nat. Commun.* **2021**, *12* (1), 4480.

(5) Watanabe, K.; Taniguchi, T.; Kanda, H. Direct-Bandgap Properties and Evidence for Ultraviolet Lasing of Hexagonal Boron Nitride Single Crystal. *Nat. Mater.* **2004**, *3* (6), 404−409.

(6) Cassabois, G.; Valvin, P.; Gil, B. Hexagonal Boron Nitride Is an Indirect Bandgap Semiconductor. *Nat. Photonics* **2016**, *10* (4), 262−266.

(7) Maciaszek, M.; Razinkovas, L.; Alkauskas, A. Thermodynamics of Carbon Point Defects in Hexagonal Boron Nitride. *Phys. Rev. Mater.* **2022**, *6* (1), 014005.

(8) Kim, S. H.; Park, K. H.; Lee, Y. G.; Kang, S. J.; Park, Y.; Kim, Y. D. Color Centers in Hexagonal Boron Nitride. *Nanomaterials* **2023**, *13* (16), 2344.

(9) Gottscholl, A.; Kianinia, M.; Soltamov, V.; Orlinskii, S.; Mamin, G.; Bradac, C.; Kasper, C.; Krambrock, K.; Sperlich, A.; Toth, M.; et al. Initialization and Read-out of Intrinsic Spin Defects in a van der Waals Crystal at Room Temperature. *Nat. Mater.* **2020**, *19* (5), 540−545.

(10) Kianinia, M.; White, S.; Fröch, J. E.; Bradac, C.; Aharonovich, I. Generation of Spin Defects in Hexagonal Boron Nitride. *ACS Photonics* **2020**, *7* (8), 2147−2152.

(11) Suzuki, T.; Yamazaki, Y.; Taniguchi, T.; Watanabe, K.; Nishiya, Y.; Matsushita, Y.; Harii, K.; Masuyama, Y.; Hijikata, Y.; Ohshima, T. Spin Property Improvement of Boron Vacancy Defect in Hexagonal Boron Nitride by Thermal Treatment. *Appl. Phys. Express* **2023**, *16* (3), 032006.

(12) Zabelotsky, T.; Singh, S.; Haim, G.; Malkinson, R.; Kadkhodazadeh, S.; Radko, I. P.; Aharonovich, I.; Steinberg, H.; Berg-Sørensen, K.; Huck, A.; et al. Creation of Boron Vacancies in Hexagonal Boron Nitride Exfoliated from Bulk Crystals for Quantum Sensing. *ACS Appl. Nano Mater.* **2023**, *6* (23), 21671−21678.

(13) Sarkar, S.; Xu, Y.; Mathew, S.; Lal, M.; Chung, J.-Y.; Lee, H. Y.; Watanabe, K.; Taniguchi, T.; Venkatesan, T.; Gradečak, S. Identifying Luminescent Boron Vacancies in h-BN Generated Using Controlled He^+ Ion Irradiation. *Nano Lett.* **2024**, *24* (1), 43−50.

(14) Tran, T. T.; Bray, K.; Ford, M. J.; Toth, M.; Aharonovich, I. Quantum Emission from Hexagonal Boron Nitride Monolayers. *Nat. Nanotechnol.* **2016**, *11* (1), 37−41.

(15) Martínez, L. J.; Pelini, T.; Waselowski, V.; Maze, J. R.; Gil, B.; Cassabois, G.; Jacques, V. Efficient Single Photon Emission from a High-Purity Hexagonal Boron Nitride Crystal. *Phys. Rev. B* **2016**, *94* (12), 121405.

(16) Silly, M. G.; Jaffrennou, P.; Barjon, J.; Lauret, J. S.; Ducastelle, F.; Loiseau, A.; Obraztsova, E.; Attal-Tretout, B.; Rosencher, E. Luminescence Properties of Hexagonal Boron Nitride: Cathodoluminescence and Photoluminescence Spectroscopy Measurements. *Phys. Rev. B* **2007**, *75* (8), 085205.

(17) Weston, L.; Wickramaratne, D.; Mackoit, M.; Alkauskas, A.; Van de Walle, C. G. Native Point Defects and Impurities in Hexagonal Boron Nitride. *Phys. Rev. B* **2018**, *97* (21), 214104.

(18) Mackoit-Sinkevičienė, M.; Maciaszek, M.; Van de Walle, C. G.; Alkauskas, A. Carbon Dimer Defect as a Source of the 4.1 eV Luminescence in Hexagonal Boron Nitride. *Appl. Phys. Lett.* **2019**, *115* (21), 212101.

(19) Jara, C.; Rauch, T.; Botti, S.; Marques, M. A. L.; Norambuena, A.; Coto, R.; Castellanos-Águila, J. E.; Maze, J. R.; Munoz, F. First-Principles Identification of Single Photon Emitters Based on Carbon Clusters in Hexagonal Boron Nitride. *J. Phys. Chem. A* **2021**, *125* (6), 1325−1335.

(20) Plo, J.; Pershin, A.; Li, S.; Poirier, T.; Janzen, E.; Schutte, H.; Tian, M.; Wynn, M.; Bernard, S.; Rousseau, A.; et al. Isotope Substitution and Polytype Control for Point Defects Identification: The Case of the Ultraviolet Color Center in Hexagonal Boron Nitride. *Phys. Rev. X* **2025**, *15* (2), 021045.

(21) Gale, A.; Li, C.; Chen, Y.; Watanabe, K.; Taniguchi, T.; Aharonovich, I.; Toth, M. Site-Specific Fabrication of Blue Quantum Emitters in Hexagonal Boron Nitride. *ACS Photonics* **2022**, *9* (6), 2170−2177.

(22) Gale, A.; Scognamiglio, D.; Zhigulin, I.; Whitefield, B.; Kianinia, M.; Aharonovich, I.; Toth, M. Manipulating the Charge State of Spin Defects in Hexagonal Boron Nitride. *Nano Lett.* **2023**, *23* (13), 6141−6147.

(23) Bozanic, A.; Petravic, M.; Fan, L. J.; Yang, Y. W.; Chen, Y. Direct Observation of Defect Levels in Hexagonal BN by Soft X-Ray Absorption Spectroscopy. *Chem. Phys. Lett.* **2009**, *472* (4), 190−193.

(24) Peter, R.; Bozanic, A.; Petravic, M.; Chen, Y.; Fan, L. J.; Yang, Y. W. Formation of Defects in Boron Nitride by Low Energy Ion Bombardment. *J. Appl. Phys.* **2009**, *106* (8), 083523.

(25) Jin, C.; Lin, F.; Suenaga, K.; Iijima, S. Fabrication of a Freestanding Boron Nitride Single Layer and Its Defect Assignments. *Phys. Rev. Lett.* **2009**, *102* (19), 195505.

(26) Cretu, O.; Ishizuka, A.; Yanagisawa, K.; Ishizuka, K.; Kimoto, K. Atomic-Scale Electrical Field Mapping of Hexagonal Boron Nitride Defects. *ACS Nano* **2021**, *15* (3), 5316−5321.

(27) Liang, H.; Chen, Y.; Loh, L.; Cheng, N. L. Q.; Litvinov, D.; Yang, C.; Chen, Y.; Zhang, Z.; Watanabe, K.; Taniguchi, T.; et al. Site-Selective Creation of Blue Emitters in Hexagonal Boron Nitride. *ACS Nano* **2025**, *19* (15), 15130−15138.

(28) Exarhos, A. L.; Hopper, D. A.; Patel, R. N.; Doherty, M. W.; Bassett, L. C. Magnetic-Field-Dependent Quantum Emission in Hexagonal Boron Nitride at Room Temperature. *Nat. Commun.* **2019**, *10* (1), 222.

(29) Attaccalite, C.; Bockstedte, M.; Marini, A.; Rubio, A.; Wirtz, L. Coupling of Excitons and Defect States in Boron-Nitride Nanostructures. *Phys. Rev. B* **2011**, *83* (14), 144115.

(30) Zhang, H.; Lan, M.; Tang, G.; Chen, F.; Shu, Z.; Chen, F.; Li, M. Discrete Color Centers in Two-Dimensional Hexagonal Boron Nitride Induced by Fast Neutron Irradiation. *J. Mater. Chem. C* **2019**, *7* (39), 12211−12216.

(31) Ivády, V.; Barcza, G.; Thiering, G.; Li, S.; Hamdi, H.; Chou, J.-P.; Legeza, Ö.; Gali, A. Ab Initio Theory of the Negatively Charged

https://doi.org/10.1021/acs.nanolett.5c02988
Nano Lett. XXXX, XXX, XXX−XXX

Boron Vacancy Qubit in Hexagonal Boron Nitride. *npj Comput. Mater.* **2020**, *6* (1), 41.
(32) Asano, T.; Tezura, M.; Saitoh, M.; Tanaka, H.; Kikkawa, J.; Kimoto, K. Nanoscale Observation of Subgap Excitations in β-Si_3N_4 with a High Refractive Index Using Low-Voltage Monochromated STEM: A New Approach to Analyze the Physical Properties of Defects in Dielectric Materials. *Appl. Phys. Express* **2022**, *15* (7), 076501.
(33) Yamashita, S.; Fukushima, S.; Kikkawa, J.; Arai, R.; Kanitani, Y.; Kimoto, K.; Kudo, Y. Local Defect and Mid-Gap State Analysis of GaN Using Monochromated EELS Combined with Nanodiffraction and Atomic-Resolution Imaging. *APL Mater.* **2024**, *12* (3), 031101.
(34) Wang, S.; March, K.; Ponce, F. A.; Rez, P. Identification of Point Defects Using High-Resolution Electron Energy Loss Spectroscopy. *Phys. Rev. B* **2019**, *99* (11), 115312.
(35) Browning, N. D.; Pennycook, S. J. Direct Experimental Determination of the Atomic Structure at Internal Interfaces. *J. Phys. D: Appl. Phys.* **1996**, *29* (7), 1779.
(36) Kimoto, K.; Kothleitner, G.; Grogger, W.; Matsui, Y.; Hofer, F. Advantages of a Monochromator for Bandgap Measurements Using Electron Energy-Loss Spectroscopy. *Micron* **2005**, *36* (2), 185−189.
(37) Egerton, R. F. *Electron Energy-Loss Spectroscopy in the Electron Microscope*; Springer Science+Business Media, LLC: 2011.
(38) Chen, C. H.; Silcox, J. Calculations of the Electron-Energy-Loss Probability in Thin Uniaxial Crystals at Oblique Incidence. *Phys. Rev. B* **1979**, *20* (9), 3605−3614.
(39) Kikkawa, J.; Taniguchi, T.; Kimoto, K. Nanometric Phonon Spectroscopy for Diamond and Cubic Boron Nitride. *Phys. Rev. B* **2021**, *104* (20), L201402.
(40) Laturia, A.; Van de Put, M. L.; Vandenberghe, W. G. Dielectric Properties of Hexagonal Boron Nitride and Transition Metal Dichalcogenides: From Monolayer to Bulk. *npj 2D Mater. Appl.* **2018**, *2* (1), 6.
(41) Haruta, M.; Fujiyoshi, Y.; Nemoto, T.; Ishizuka, A.; Ishizuka, K.; Kurata, H. Extremely Low Count Detection for EELS Spectrum Imaging by Reducing CCD Read-out Noise. *Ultramicroscopy* **2019**, *207*, 112827.
(42) Haruta, M.; Kikkawa, J.; Kimoto, K.; Kurata, H. Comparison of Detection Limits of Direct-Counting CMOS and CCD Cameras in EELS Experiments. *Ultramicroscopy* **2022**, *240*, 113577.
(43) Taniguchi, T.; Watanabe, K. Synthesis of High-Purity Boron Nitride Single Crystals under High Pressure by Using Ba−BN Solvent. *J. Cryst. Growth* **2007**, *303* (2), 525−529.
(44) McDougall, N. L.; Partridge, J. G.; Nicholls, R. J.; Russo, S. P.; McCulloch, D. G. Influence of Point Defects on the near Edge Structure of Hexagonal Boron Nitride. *Phys. Rev. B* **2017**, *96* (14), 144106.
(45) Browning, N. D.; Yuan, J.; Brown, L. M. Theoretical Determination of Angularly-Integrated Energy-Loss Functions for Anisotropic Materials. *Philos. Mag. A* **1993**, *67* (1), 261−271.
(46) Fraunié, J.; Clua-Provost, T.; Roux, S.; Mu, Z.; Delpoux, A.; Seine, G.; Lagarde, D.; Watanabe, K.; Taniguchi, T.; Marie, X.; et al. Charge State Tuning of Spin Defects in Hexagonal Boron Nitride. *Nano Lett.* **2025**, *25* (14), 5836−5842.
(47) Clua-Provost, T.; Mu, Z.; Durand, A.; Schrader, C.; Happacher, J.; Bocquel, J.; Maletinsky, P.; Fraunié, J.; Marie, X.; Robert, C.; et al. Spin-Dependent Photodynamics of Boron-Vacancy Centers in Hexagonal Boron Nitride. *Phys. Rev. B* **2024**, *110* (1), 014104.
(48) Baber, S.; Malein, R. N. E.; Khatri, P.; Keatley, P. S.; Guo, S.; Withers, F.; Ramsay, A. J.; Luxmoore, I. J. Excited State Spectroscopy of Boron Vacancy Defects in Hexagonal Boron Nitride Using Time-Resolved Optically Detected Magnetic Resonance. *Nano Lett.* **2022**, *22* (1), 461−467.
(49) Whitefield, B.; Toth, M.; Aharonovich, I.; Tetienne, J.-P.; Kianinia, M. Magnetic Field Sensitivity Optimization of Negatively Charged Boron Vacancy Defects in hBN. *Adv. Quantum Technol.* **2025**, *8* (4), 2300118.
(50) Lee, W.; Liu, V. S.; Zhang, Z.; Kim, S.; Gong, R.; Du, X.; Pham, K.; Poirier, T.; Hao, Z.; Edgar, J. H.; et al. Intrinsic High-Fidelity Spin Polarization of Charged Vacancies in Hexagonal Boron Nitride. *Phys. Rev. Lett.* **2025**, *134* (9), 096202.

https://doi.org/10.1021/acs.nanolett.5c02988
Nano Lett. XXXX, XXX, XXX−XXX